Analytical Crack Model Inferred from Contained Laboratory-Generated Earthquakes

Chun-Yu Ke[1], Gregory C. McLaskey[1] and David S. Kammer[2]

[1]*School of Civil and Environmental Engineering, Cornell University, Ithaca, New York, USA*

[2]*Institute for Building Materials, ETH, Zürich, Switzerland. E-mail: dkammer@ethz.ch*

31 October 2019

This is a non-peer reviewed preprint submitted to EarthArXiv.

It has been submitted for review to Geophys. J. Int. on October 25, 2019.

SUMMARY

Earthquake ruptures are generally considered to be cracks that propagate as fracture or frictional slip on preexisting faults. Crack models have been used to describe the spatial distribution of fault offset and the associated static stress changes along a fault, and have implications for friction evolution and the underlying physics of rupture processes. However, measurements that could help refine idealized crack models are rare. Here we describe large-scale laboratory earthquake experiments, where all rupture processes were contained within a 3-m long saw-cut granite fault, and we propose an analytical crack model that fits our measurements. Similar to natural earthquakes, laboratory measurements of displacements show coseismic slip that gradually tapers near the rupture tips. Measured stress changes show a roughly constant stress drop within the ruptured region, and a smooth transition from residual to peak stress near the rupture tips. The proposed crack model generalizes the widely used elliptical crack model by adding a cohesive zone that eliminates the unrealistic stress singularity at the rupture tip.

Key words: Friction; Mechanics, theory, and modelling; Spatial analysis.

1 INTRODUCTION

Earthquakes are commonly modeled as shear cracks, where the slip profile of an earthquake rupture is the spatial distribution of displacement discontinuity between the fault surfaces. It is the accumulated result of any slip that occurs during quasi-static nucleation (Dieterich 1992; Uenishi & Rice 2003), dynamic rupture propagation (Madariaga 1976; Passelègue *et al.* 2013), and rapid post-seismic slip (Freed *et al.* 2010; Wei *et al.* 2015). The slip profile during a single earthquake is related to the spatial distribution of on-fault stress changes associated with the rupture. It is therefore important for understanding the mechanics of earthquakes and has implications for stress drop, stress redistribution, and earthquake-to-earthquake triggering (Freed 2005).

Most analytical models of slip profiles focus on simplicity for application purposes. For instance, the linear elastic crack model (Bilby & Eshelby 1968) established that a perfect crack with uniform shear stress drop within the rupture area leads to an elliptical slip profile (Fig. 1). This elliptical model casts infinite stress at the rupture tips, which is unrealistic because real interfaces have finite strength. In order to keep stresses finite, the slip distance must taper off more gradually near the rupture tips. Cowie & Scholz (1992) and Bürgmann *et al.* (1994) adapted the Dugdale model (Dudgale 1960) and applied it to a mode II crack with constant-stress cohesive zones near the rupture tips, which results in bell-shaped slip profiles (Fig. 1). This may be an adequate model to approximate faulting processes by assuming perfectly plastic failure, however, its uniform stress and strength assumption is not always valid. Numerical models have been proposed in order to accomondate irregular shapes of slip profiles (*e.g.,* Bürgmann *et al.* 1994; Manighetti *et al.* 2004; Scholz & Lawler 2004), and arbitary forms of cohesive zones around the rupture tip (Ida 1972), where stresses smoothly transition from residual to peak strength in a relatively short distance compared to the total rupture length. Slip at the rupture tips is small and difficult to measure, but can have a strong influence on stress concentrations. In this work, we use measurements of laboratory earthquakes to illuminate the features of earthquake slip profiles, including the cohesive zone.

Most past field studies of fault slip distributions provide information relevant to the growth of brittle faults over many earthquakes or slow slip events. When considering slip profiles from

individual events, measured slip distributions are often so heterogeneous that stacking of many individual events is required to evaluate features. Using this approach, Manighetti *et al.* (2005) found that slip distributions derived from kinematic models and field observations were roughly triangular and predominantly asymmetric. Studies of faulting showed that slip gradients appeared approximately constant near the fault tip (Muraoka & Kamata 1983; Walsh & Watterson 1987; Dawers *et al.* 1993; Nicol *et al.* 1996; Manighetti *et al.* 2001). Walsh & Watterson (1987) argued that the ubiquitous linear tapering feature of slip profiles can be an artifact of cumulative slips from multiple growing cracks with elliptical shape. This argument hightlights the difficulty of distingushing the field measurements of slip profile accumulated across multiple earthquake ruptures and of a single earthquake rupture, which will result in very different shapes and possibly different conclusions.

Here we present results from recent large-scale laboratory experiments where the rupture processes are partially or completely contained in a 3-meter long saw-cut granite fault (Ke *et al.* 2018; Wu & McLaskey 2019). This provides a unique opportunity to measure local slip and local static shear stress changes along the simulated fault near the rupture tip. We propose an analytical crack model that explains our experimental data and accomondates most of the aforementioned naturally observed features while adhering the associated stress changes to physical constraints.

2 SPATIAL DISTRIBUTION OF STRESS CHANGES

For a mode II (in-plane shear) crack, we define the spatial distribution of shear stress change associated with an earthquake rupture as $\Delta\tau(x) \equiv \tau_{\mathrm{f}}(x) - \tau_0(x)$, where $\tau_0(x)$ is the spatial distribution of shear stress at the (quasi-)static state before the rupture nucleates and $\tau_{\mathrm{f}}(x)$ is the spatial distribution of shear stress at the (quasi-)static state after the rupture arrests. Thus, $\Delta\tau(x)$ is the shear stress changes due to all processes of a rupture between two (quasi-)static states. Bilby & Eshelby (1968) derived the constitutive relationship between the distribution of slip parallel to the fault $\delta(x)$ and shear stress change distribution $\Delta\tau(x)$,

$$\Delta\tau(x) = -\frac{\mu^*}{2\pi}\int_{a_-}^{a_+}\frac{d\delta(\xi)/d\xi}{x-\xi}d\xi, \tag{1}$$

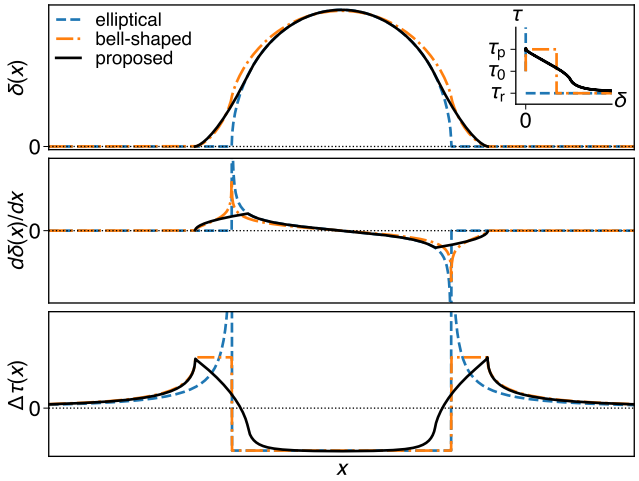

Figure 1. Examples of crack models' slip profile $\delta(x)$, first derivative of slip profile $d\delta(x)/dx$, and associated shear stress changes $\Delta\tau(x)$. The elliptical model has singularities in $d\delta(x)/dx$, which also results in singularities in $\Delta\tau$ at rupture tips. The bell-shaped model is designed to have the maximum shear stress limited, casting a constant $\Delta\tau$ plateau near rupture tips under uniform stress and strength field. The proposed model preserves the elliptical slip profile in the center and swaps the edges of the crack with $x^{3/2}$ form, effectively eliminating shear stress singularities while keeping $\Delta\tau(x)$ nonsingularly peaks at rupture tips with variable cohesive zones. The inset depicts the τ-δ relationship of all three models, where τ_0 is the initial stress, τ_p is the peak strength, and τ_r is the residual strength.

where $\mu^* = \mu/(1-\nu)$ for mode II, in which μ is the shear modulus and ν is the Poisson's ratio, and $a_\pm$ are the locations of the rupture tips. This equation assumes the material surrounding the rupture is linear elastic. It takes the first derivative of the slip profile $d\delta(x)/dx$ as input and gives its respective static stress change distribution $\Delta\tau(x)$. Note that if a given $\delta(x)$ is C^1 continuous and $\delta(x) \sim (\pm[a_\pm - x])^{3/2}$ as x approaches $a_\pm$ within the rupture, its respective $\Delta\tau(x)$ is smooth and finite (see Uenishi & Rice (2003): Appendix A).

The two classical crack models, elliptical and bell-shaped slip profiles, have been widely used due to their analytical nature (Scholz 2019), but both are idealized and thus may not capture all revelent aspects of earthquake ruptures. The $d\delta(x)/dx$ of the elliptical slip profile approaches $\pm\infty$ at the rupture tips and thus $\Delta\tau(x)$ approaches $+\infty$ (Fig. 1), which is not physical because materials or frictional interfaces have finite strength. The bell-shaped slip profile (Cowie & Scholz 1992; Bürgmann *et al.* 1994) assumes τ reaches the peak strength τ_p and stays at the peak strength near rupture tips (Fig. 1). However, this constant-stress cohesive zone near the rupture tip is not

observed in our experiments, or is smaller than the spatial resolution of our strain measurements (10 cm). Note that if the constant-stress cohesive zone width approaches zero, the bell-shaped model reduces into the elliptical model. Both the elliptcal model and the bell-shaped model have a spatial discontinuity in $\Delta\tau(x)$ at/near the rupture tips, which jumps from the residual strength τ_{r} to $+\infty$ and τ_{p}, respectively. On the other hand, $\Delta\tau(x)$ appears to transition smoothly near the crack tips in our experiments, as we will show in Section 6. This discontinuity is also at odds with current understanding of friction evolution when plotted in the τ-δ graph, as shown in Fig. 1 (inset), where the frictional strength should weaken from τ_{p} to τ_{r} continuously over a finite amount of slip (Palmer & Rice 1973). Moreover, both models assume uniform stress and strength across the fault length. The heterogeneity in the spatial distribution of stress and strength can strongly affect the geometry of a rupture. In our experiments, ruptures terminate due to entering a region where the initial stress τ_0 gradually transitions below the residual strength τ_{r} (Ke *et al.* 2018), which presumably smoothens the cohesive zones. Therefore, the uniform stress and strength assumptions are not reasonable near the rupture tips for our applications.

3 PROPOSED CRACK MODEL

We derived an expression that combines the elliptical shape in the center of the rupture and an $r^{3/2}$ form at the edges, which replaces stress singularties in the elliptical model with mathematically simplistic cohesive zones. The edges of the slip profile are approximately linear (Fig. 1), consistent with slip profiles obtained from natural faults. The proposed analytical model of slip profiles is formulated as

$$\delta(r) = \begin{cases} D\left[1-\left(\frac{r}{\lambda a}\right)^2\right]^{1/2} & ,0 \le r \le r^{\mathrm{joint}} \\ \delta^{\mathrm{joint}}\left(\frac{r-a}{r^{\mathrm{joint}}-a}\right)^{3/2} & ,r^{\mathrm{joint}} < r \le a \\ 0 & ,a < r \end{cases} \tag{2}$$

where r is the distance to the center of the crack, a is the radius of the crack, λ scales a to the radius of the ellipse $a^{\mathrm{ellipse}} = \lambda a$, in which $0 < \lambda < 1$, $r^{\mathrm{joint}} = \left(\sqrt{1+3\lambda^2}-1\right)a$ is the radius where $\delta(r)$ switches between elliptical and $r^{3/2}$ form, and $\delta^{\mathrm{joint}} = \delta(r^{\mathrm{joint}})$. Compared to the elliptical (or ellipsoidial) model, $\delta(r) = D\left[1-\left(\frac{r}{a}\right)^2\right]^{1/2}$ for $0 \le r \le a$, this model introduces only one

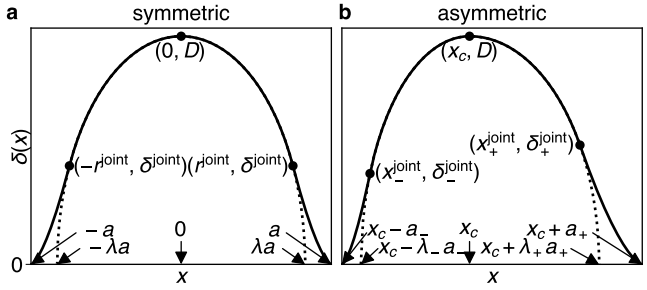

Figure 2. Parameters of the proposed slip profile model in one-dimentional (a) symmetric form (Equation 2) and (b) asymmetric form (Equation 3). (a) Dotted curve shows the elliptical model this model follows between $\pm r^{\text{joint}}$ with radius λa and height $\delta(0) = D$, in which a is the half-length of the rupture and $0 < \lambda < 1$. (b) Dotted curve shows the assymetric elliptical model this model follows between $x_{\pm}^{\text{joint}}$ with radius $\lambda_{\pm} a_{\pm}$ on either side of x_c, in which x_c is the location such that $\delta(x_c) = D$, $x_c \pm a_{\pm}$ are the locations of rupture tips $x_{\pm}^{\text{tip}}$.

additional parameter, λ, and guarantees C^1 continuity in $\delta(r)$ and no singulatity in the associated stress changes if $0 < \lambda < 1$. Note that this model reduces into the elliptical model if $\lambda = 1$.

We extend the model to an asymmetrical formulation in a one-dimentional coordinate system (x) by introducing a new parameter x_c as the location of the maximum δ and repeating a and λ on either side of x_c,

$$\delta(x) = \begin{cases} \delta_-^{\text{joint}} \left(\frac{x - x_-^{\text{tip}}}{x_-^{\text{joint}} - x_-^{\text{tip}}} \right)^{3/2} & , x_-^{\text{tip}} < x < x_-^{\text{joint}} \\ D \left[1 - \left(\frac{x - x_c}{\lambda_- a_-} \right)^2 \right]^{1/2} & , x_-^{\text{joint}} \leq x < 0 \\ D \left[1 - \left(\frac{x - x_c}{\lambda_+ a_+} \right)^2 \right]^{1/2} & , 0 \leq x \leq x_+^{\text{joint}} \\ \delta_+^{\text{joint}} \left(\frac{x_+^{\text{tip}} - x}{x_+^{\text{tip}} - x_+^{\text{joint}}} \right)^{3/2} & , x_+^{\text{joint}} < x < x_+^{\text{tip}} \\ 0 & , \text{otherwise} \end{cases} \tag{3}$$

where x_c is the location of maximum δ such that $\delta(x_c) = D$, $a_{\pm}$ are the rupture half-lengths on either side of x_c, $x_{\pm}^{\text{tip}} = x_c \pm a_{\pm}$ are the locations of rupture tips, $\lambda_{\pm}$ controls the radius of the ellipse $a_{\pm}^{\text{ellipse}} = \lambda_{\pm} a_{\pm}$, in which $0 < \lambda_{\pm} < 1$, $x_{\pm}^{\text{joint}} = x_c \pm \left(\sqrt{1 + 3\lambda_{\pm}^2} - 1 \right) a_{\pm}$ are the locations where $\delta(x)$ switches between elliptical and $(\pm[a_{\pm} - x])^{3/2}$ forms, and $\delta_{\pm}^{\text{joint}} = \delta(x_{\pm}^{\text{joint}})$.

4 EXPERIMENTAL METHODS AND MEASUREMENTS

Experiments were conducted on a biaxial direct shear apparatus as shown in Fig. 3. Slip events occurred on the simulated fault as shear load increased. The dimensions of the moving block and the stationary block are 3.10 m $\times$ 0.81 m $\times$ 0.30 m, and 3.15m $\times$ 0.61 m $\times$ 0.30 m (respectively) in the x, y, and z directions. The dimensions of the simulated fault are 3.10 m $\times$ 0.30 m with area $A = 0.95\ \mathrm{m}^2$. The fault surfaces of the granite samples were prepared by the manufacturer to be flat and parallel to 125 μm. Mechanical properties of the Barre Gray granite are E = 30 GPa and ν = 0.23.

The normal loading array, consisting of 18×2 hydraulic cylinders, presses two rock blocks together in the y-direction and applies normal contact pressure on the fault. The shear loading array, consisting of 6×3 hydraulic cylinders, pushes the moving block in $+x$-direction and applies shear stress on the fault. Hydraulic cylinders in each array are interconnected to a manual pump, allowing us to independently control normal and shear loading. The measurements of hydraulic pressure in both arrays are then converted and reported as sample average normal and shear stress, $\bar{\sigma}$ and $\bar{\tau}$.

Local fault slip was measured by 16 evenly spaced eddy current displacement sensors at 16 locations (E_1–E_{16}) along the fault as shown in Fig. 3. These sensors measure the relative displacement between each side of the fault, *i.e.*, the moving rock block and the stationary rock block. Local shear strain was measured by 16 pairs (S_1–S_{16}) of semiconductor strain gages at locations shown in Fig. 3, with S_{11} and E_{11} being collocated and all others evenly spaced between E_1–E_{16}. Each pair consists of two collocated 4 mm long semiconductor strain gages oriented at 45° and 135° from the fault which were glued to the moving block, 5 mm from the fault. Local shear stress τ was derived from measurements of the strain gage pair and the elastic properties of Barre Gray granite. While the 5 mm off-fault measurement can be biased for dynamic responses (Svetlizky & Fineberg 2014; Kammer & McLaskey 2019), we assume negligible differences between on-fault and 5 mm off-fault measurements when at (quasi-)static stress states.

Before every experiment, we apply $\bar{\sigma} \approx 1$ MPa and then increase τ until the whole simulated fault slips a few times to create a consistent initial stress distribution for the following procedures.

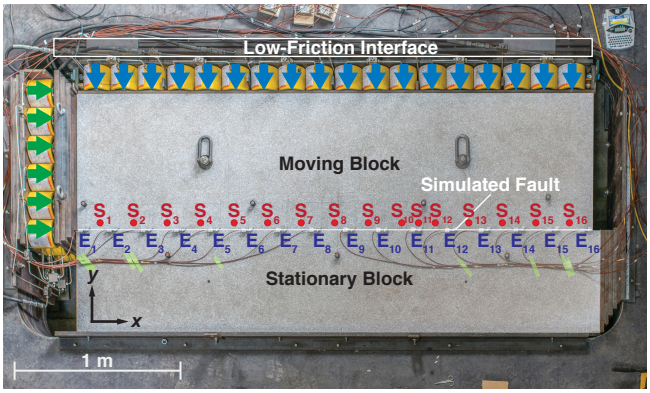

Figure 3. Experimental setup. The moving block and the stationary block were pressed together to compose the simulated fault of granite. A low friction interface consisted of a 2.4 mm thick sheet of reinforced Teflon sliding on precision ground steel plates ($\mu \approx 0.1$) allows the normal loading array (blue arrows) to translate with the moving block in the x-direction. Shear loading array (green arrows) pushes the moving block in the x-direction to apply shear stress and induce ruptures on the simulated fault. S_1–S_{16} show the locations of 16 sets of strain gage pairs and E_1–E_{16} show the locations of 16 slip sensors.

During the experiments, normal load was first increased to the prescribed level $\bar{\sigma}_0$ and a valve was closed to keep the volume of hydraulic fluid in the normal loading array constant. Shear load was then increased at a roughly constant rate to induce sequences of slip events. In this work we study individual slip events. Further information about the experimental setup, procedures, and mechanics of the sequences can be found in Ke *et al.* (2018) and Wu & McLaskey (2019).

5 DETERMINATION OF $\delta(x)$ AND $\Delta\tau(x)$

In our experiments, slow fault creep and nucleation-related slow slip sometimes occures prior to and after slip events, as shown in Fig. 4a. For these events, using a smaller time window to calculate δ and $\Delta\tau$ could exclude quasi-static nucleation process and result in incomplete $\delta(x)$ and $\Delta\tau(x)$, as shown in Fig. 4b. On the other hand, using a larger time window that includes the nucleation process and after slip will also include stress changes from the slow and continuous loading and slip from quasi-static steady slow slip. We account for these slow processes by fitting linear trends in time histories before and after the dynamic rupture process then extrapolating the linear time histories to the instant of the dynamic rupture process and take differences to define the δ and $\Delta\tau$

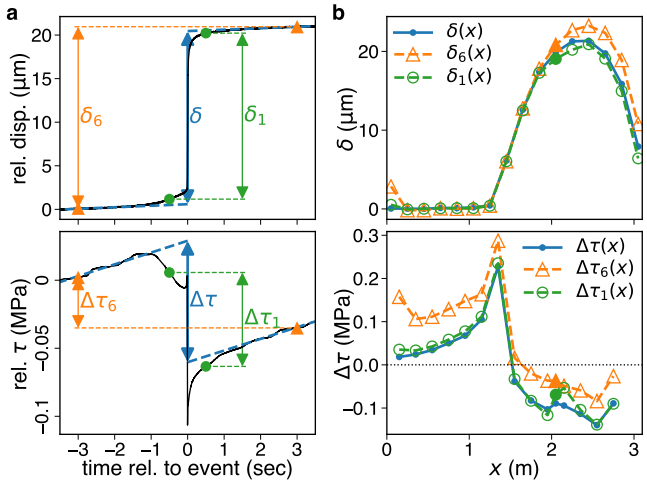

Figure 4. Example of slip and stress change time histories and extracted δ and $\Delta\tau$ from FS01-038-7MPa-P-1-03 event. (a) Heavy dashed lines are linear trends associated with continuous loading and fitted from data before (t = -3 to -2 sec) and after (t = 2 to 3 sec) the event. Parameters δ and $\Delta\tau$ are then defined by the difference between linear trends before and after the event extrapolated to instant of dynamic rupture (t = 0) as shown. δ_6 and $\Delta\tau_6$ are defined by the difference with a 6-second time window, *i.e.*, difference between $t = \pm 3$ second. Similarly, δ_1 and $\Delta\tau_1$ are defined by the difference with a 1-second time window. (b) Solid curves are results of $\delta(x)$ and $\Delta\tau(x)$ with linear trends removed. Dashed curves are estimates made without linear trends removed. The estimate from a 6-s window, $\delta_6(x)$, is slightly larger than $\delta_1(x)$ due to the inclusion of quasi-static slip during nucleation and after slip. Similarly, $\Delta\tau_6 > \Delta\tau_1(x)$ due to the inclusion of stress changes associated with continuous loading. Note that the deviations near x = 2 m in both $\delta_1(x)$ and $\Delta\tau_1(x)$ were due to the exclusion of the quasi-static nucleation process.

associated with a dynamic slip event from each location (Fig. 4). Events with fast nucleation and no after slip are unaffected by the above procedure.

6 RESULTS

Fig. 5a shows slip profiles and associated stress changes measured from contained laboratory-generated earthquakes and the respective model fits. The proposed model describes well both the slip profile and the associated stress changes. The spatial resolution of slip profile $\delta(x)$ measurements is arguably not high enough to resolve the fine details near the rupture tips. However, $\Delta\tau(x)$ is very sensitive to the (nonlocal) details of $\delta(x)$, therefore measurements of $\Delta\tau(x)$ can provide additional data to guide and resolve the fine details in $\delta(x)$ near the rupture tips. From Equation 1, we know that $\Delta\tau(x)$ depends on $d\delta(x)/dx$, which means a slight deviation of $\delta(x)$ near the

rupture tips can strongly affect the associated $\Delta\tau(x)$. Thus, fitting slip measurements to a slip profile model is a more robust way to resolve $\delta(x)$ and the associated $\Delta\tau(x)$ of earthquake ruptures compared to interpolating between sparse data points of $\delta(x)$ measurements and then calculating $d\delta(x)/dx$ and the associated $\Delta\tau(x)$.

Example events on the top row of Fig. 5 are completely contained ruptures. Model fits involved 6 free parameters, D, x_c, $a_{\pm}$, and $\lambda_{\pm}$. The number of data points of $\delta(x)$ and $\Delta\tau(x)$ within the extent of the smallest rupture we obtained still exceeds the number of model parameters. Moreover, we find the proposed model also fits well partially contained ruptures, where only one end of the rupture arrested inside the simulated fault and the other end propagated to the edge of the sample, as shown on the bottom row of Fig. 5, in which model fits involved 4 free parameters, D, x_c, a, and λ.

Fig. 5b shows two relatively large rupture events from our experiments, which have more data points in the ruptured area, to demonstrate the quality of model fits of the elliptical model, the bell-shaped model, and the proposed model. Since the bell-shaped model is not formulated to be stretched assymetrically, we sliced slip profiles in half with respect to the location of maximum δ for the comparison between three models. For both events, completely and partially contained ruptures, all 3 models fit $\delta(x)$ well. However, a more important index of the quality of model fits is the shape of $\Delta\tau(x)$ near the rupture tip, *i.e.*, the cohesive zone. For events that have strain measurements located within the cohesive zones, $\Delta\tau(x)$ always shows a smooth transition from the interior to the edge and nonsingularly peaks at the rupture tip instead of plateaus. Of the 24 completely contained ruptures and 13 partially contained ruptures studied here, the coefficient of determination R^2 of $\delta(x)$ and $\Delta\tau(x)$ fits are $97.7\% \pm 2.3\%$ and $83.7\% \pm 10.7\%$, respectively. Our experiments show that the proposed model more closely matches the shape of the associated $\Delta\tau(x)$ near the rupture tips compared to the other two analytical slip profile models. Even though the spatial resolution of strain measurements is not high enough to verify the exact shape of $\Delta\tau(x)$ at the cohesive zone, the proposed model provides a first order approximation to the smooth transition of $\Delta\tau(x)$ from dynamic rupture propagation to termination.

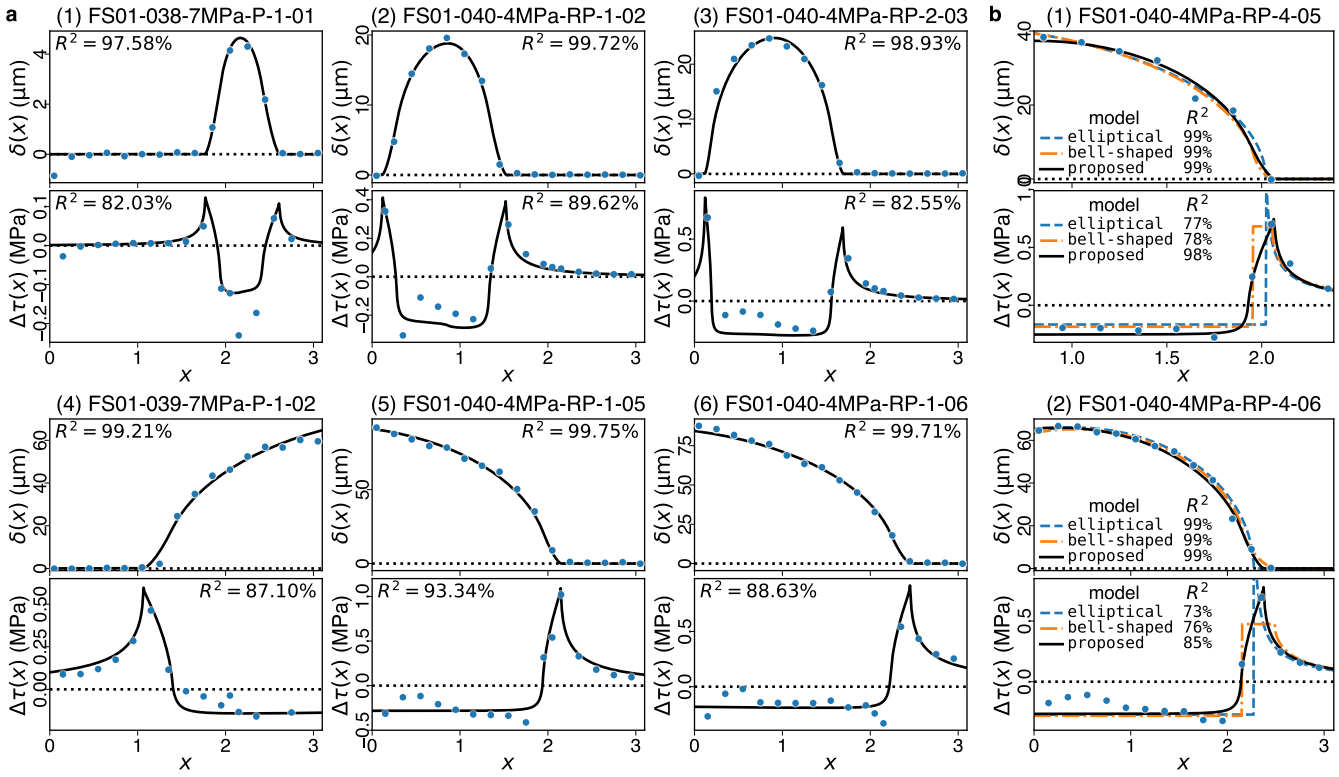

Figure 5. Examples of measured rupture events and model fits. (a) Blue dots indicate measurements of $\delta(x)$ and $\Delta\tau(x)$. Solid curves are results of model fits. The coefficient of determination R^2 of model fits is marked next to each curve. (b) Comparison between the elliptical, the bell-shaped, and the proposed model. Entries in legends denote R^2 of each model fit.

7 DISCUSSION

The proposed model merges an elliptical slip profile with an $x^{3/2}$ form at the edges. This allows constant stress drop in the center while keeping the stress concentration at rupture tips finite, and retains a smooth transition in between. Compared to the bell-shaped model, the friction cohesive zone width s described in Cowie & Scholz (1992) is identical to $a - d$ in Bürgmann *et al.* (1994), and conceptually similar to the cohesive zone width $L_{\mathrm{coh}} = \left(2 - \sqrt{1 + 3\lambda^2}\right) a$ in this model. One can use the proposed model to estimate L_{coh} of an earthquake rupture and apply it to cohesive zone theory, *e.g.*, $L_{\mathrm{coh}} = 9\pi K_{\mathrm{II}}^2 / [32(\tau_{\mathrm{p}} - \tau_{\mathrm{r}})^2]$ (Palmer & Rice 1973), to estimate the fracture energy from the respective energy release rate if the underlying uniform stress and strength assumption is reasonable. The cumulative faulting model derived by Walsh & Watterson (1987) also has the approximately linear tapering feature at edges and limited stress concentration at rupture tips, but its associated stress changes have a triangular shape. In that model, the cohesive zone is essentially

the entire rupture half-length, and the triangular shape does not match our observations or other models of single earthquake ruptures that show roughly uniform $\Delta\tau(x)$ inside the ruptured region.

It has been believed that it is the inelastic deformation in the volume around the fault tips (Cowie & Scholz 1992; Bürgmann *et al.* 1994) or the accumulation over multiple earthquake ruptures (Walsh & Watterson 1987) that caused the nearly linear taper in slip profiles. Our individual laboratory earthquakes show that slip profiles of purely frictional ruptures produce similar features as seen in natural faults. There was no sign of inelastic deformation or damage off the fault surface upon inspections on the simulated fault. The approximately linear taper at the edges of slip profiles observed in natural faults is orders of magnitude larger than the length-scale of inelastic fracture or friction processes. It is possible that this feature is predominately caused by the smooth spatial transition in stress between $\tau_0 > \tau_\mathrm{r}$ and $\tau_0 < \tau_\mathrm{r}$, similar to what we observed in our contained laboratory earthquakes (Ke *et al.* 2018).

Our contained laboratory-generated earthquakes have smoother slip profile compared to natural earthquakes. This could be because the simulated fault is more smooth and flat than natural faults. Another possibility is that ruptures entered unfavored stress conditions and terminated before the rupture front was fully dynamic (Svetlizky *et al.* 2017), and therefore more complex high-speed processes could not engage. Measurements of $\Delta\tau(x)$ inside the ruptured region, where dynamic rupture propagation took place, were slightly more deviated from the model and less smooth compared to the rest of the fault. Perhaps the ruptures are not completely homogeneous along depth while the strain gages are glued on the surface of the rock blocks, or some randomness is introduced by the rapid fluctuations in slip and stress during the dynamic rupture process as seen in a previous study with similar experimental setup (McLaskey *et al.* 2015). The values of λ from completely contained ruptures ranged from 0.49 to 0.99, with averaged value of 0.84, median of 0.85. There is no appearent trend in D and L_coh (or λ) against a since a only spans from 0.5 m to 2 m, less than one order of magnitude. The smooth transition of $\Delta\tau_\mathrm{pot}(x) \equiv \tau_0(x) - \tau_\mathrm{r}(x)$ between zero near the rupture tips causes the appearent L_coh, the width of the transition from τ_r to τ_p, to be wider than what fracture mechanics would suggest (Palmer & Rice 1973) under the uniform stress and strength assumptions. The mean value of L_coh inferred from completely contained ruptures is

0.22 m, while the theory predicts 0.0066 m assuming $\Gamma \approx 1\ \mathrm{J/m^2}$ (Ke *et al.* 2018; Kammer & McLaskey 2019) and linear slip-weakening friction law (Andrews 1976) with $d_0 = 1\ \mu\mathrm{m}$.

While the proposed model is more flexible in shapes, it might not be able to capture the overall slip profile on a complex natural fault. Instead, one can consider stacking multiple slip profiles or use the model as a basis function to better fit a given slip profile. The nature of this model's smoother and more realistic cohesive zone in $\Delta\tau(x)$ can also benefit kinematic source models, *e.g.*, Ruiz *et al.* (2011), when used to replace the elliptical model.

8 CONCLUSIONS

Our contained laboratory-generated earthquakes ruptured a nominally flat and smooth frictional interface, which almost completely eliminated heterogeneities in geometry and material properties. With only heterogeneity in stress distribution, we generated laboratory earthquakes contained within 3-meter long simulated fault, providing a rare opportunity to study important features of slip profiles and the associated stress changes in a simplified laboratory setting. In addition to local slip measurements, we also used local shear strain measurements to help resolve the details of slip profiles near the rupture tips, where stress changes are profound.

We proposed a slip profile model that does not contain the stress singularity of the elliptical model and relaxes the absolute stress upper bound of the bell-shaped model (Cowie & Scholz 1992; Bürgmann *et al.* 1994). Its analytical expression is simple yet versatile in shape, and it fits well both slip profiles and associated stress changes measured in our experiments. The laboratory measurements provide evidence for a cohesive zone, which has only be seen in numerical models before. While the full details of the cohesive zone may not have been resolved due to limited spatial resolution, this model provides a proper first-order approximation to the smooth transition from the residual strength to the peak strength. This model, motivated by physical measurements, may be useful as a component of more complicated fault rupture and rupture sequence earthquake models.

ACKNOWLEDGMENTS

This research was supported by the National Science Foundation under grant EAR-1763499. Data used in this paper were acquired during laboratory experiments conducted at Cornell University. Data reported here are publicly available at https://eCommons.cornell.edu. We thank Bill S. Wu for assistance with the experiments. The authors declare that they have no conflict of interest.

REFERENCES

Andrews, D. J., 1976. Rupture propagation with finite stress in antiplane strain, *Journal of Geophysical Research*, **81**(20), 3575.

Bilby, B. A. & Eshelby, J. D., 1968. Dislocations and the theory of fracture, in *Fracture, an Advanced Treatise*, vol. I, chap. 2, pp. 99–182, ed. Liebowitz, H., Academic, San Diego, Calif.

Bürgmann, R., Pollard, D. D., & Martel, S. J., 1994. Slip distributions on faults: effects of stress gradients, inelastic deformation, heterogeneous host-rock stiffness, and fault interaction, *Journal of Structural Geology*, **16**(12), 1675–1690.

Cowie, P. A. & Scholz, C. H., 1992. Physical explanation for the displacement-length relationship of faults using a post-yield fracture mechanics model, *Journal of Structural Geology*, **14**(10), 1133–1148.

Dawers, N. H., Anders, M. H., & Scholz, C. H., 1993. Growth of normal faults: Displacement-length scaling, *Geology*, **21**(12), 1107.

Dieterich, J. H., 1992. Earthquake nucleation on faults with rate-and state-dependent strength, *Tectonophysics*, **211**(1-4), 115–134.

Dudgale, D., 1960. Yielding of steel sheets containing slits, *Journal of the Mechanics and Physics of Solids*, **8**(2), 100–104.

Freed, A. M., 2005. Earthquake Triggering By Static, Dynamic, and Postseismic Stress Transfer, *Annual Review of Earth and Planetary Sciences*, **33**(1), 335–367.

Freed, A. M., Herring, T., & Bürgmann, R., 2010. Steady-state laboratory flow laws alone fail to explain postseismic observations, *Earth and Planetary Science Letters*, **300**(1-2), 1–10.

Ida, Y., 1972. Cohesive force across the tip of a longitudinal-shear crack and Griffith's specific surface energy, *Journal of Geophysical Research*, **77**(20), 3796–3805.

Kammer, D. S. & McLaskey, G. C., 2019. Fracture energy estimates from large-scale laboratory earthquakes, *Earth and Planetary Science Letters*, **511**, 36–43.

Ke, C.-Y., McLaskey, G. C., & Kammer, D. S., 2018. Rupture Termination in LaboratoryGenerated Earthquakes, *Geophysical Research Letters*, **45**(23), 12784–12792.

298 Madariaga, R., 1976. Dynamics of an expanding circular fault, *Bulletin of the Seismological Society of*
299 *America*, **66**(3), 639–666.
300 Manighetti, I., King, G. C. P., Gaudemer, Y., Scholz, C. H., & Doubre, C., 2001. Slip accumulation
301 and lateral propagation of active normal faults in Afar, *Journal of Geophysical Research: Solid Earth*,
302 **106**(B7), 13667–13696.
303 Manighetti, I., King, G., & Sammis, C. G., 2004. The role of off-fault damage in the evolution of normal
304 faults, *Earth and Planetary Science Letters*, **217**(3-4), 399–408.
305 Manighetti, I., Campillo, M., Sammis, C., Mai, P. M., & King, G., 2005. Evidence for self-similar, tri-
306 angular slip distributions on earthquakes: Implications for earthquake and fault mechanics, *Journal of*
307 *Geophysical Research*, **110**(B5), B05302.
308 McLaskey, G. C., Kilgore, B. D., & Beeler, N. M., 2015. Slip-pulse rupture behavior on a 2 m granite
309 fault, *Geophysical Research Letters*, **42**(17), 7039–7045.
310 Muraoka, H. & Kamata, H., 1983. Displacement distribution along minor fault traces, *Journal of Structural*
311 *Geology*, **5**(5), 483–495.
312 Nicol, A., Watterson, J., Walsh, J. J., & Childs, C., 1996. The shapes, major axis orientations and displace-
313 ment patterns of fault surfaces, *Journal of Structural Geology*, **18**(2-3), 235–248.
314 Palmer, A. C. & Rice, J. R., 1973. The Growth of Slip Surfaces in the Progressive Failure of Over-
315 Consolidated Clay, *Proceedings of the Royal Society A: Mathematical, Physical and Engineering Sci-*
316 *ences*, **332**(1591), 527–548.
317 Passelègue, F. X., Schubnel, A., Nielsen, S., Bhat, H. S., & Madariaga, R., 2013. From sub-Rayleigh to
318 supershear ruptures during stick-slip experiments on crustal rocks, *Science*, **340**(6137), 1208–1211.
319 Ruiz, J. A., Baumont, D., Bernard, P., & Berge-Thierry, C., 2011. Modelling directivity of strong ground
320 motion with a fractal, k-2, kinematic source model, *Geophysical Journal International*, **186**(1), 226–244.
321 Scholz, C. H., 2019. *The Mechanics of Earthquakes and Faulting*, Cambridge University Press, 3rd edn.
322 Scholz, C. H. & Lawler, T. M., 2004. Slip tapers at the tips of faults and earthquake ruptures, *Geophysical*
323 *Research Letters*, **31**(21), 1–4.
324 Svetlizky, I. & Fineberg, J., 2014. Classical shear cracks drive the onset of dry frictional motion, *Nature*,
325 **509**(7499), 205–208.
326 Svetlizky, I., Kammer, D. S., Bayart, E., Cohen, G., & Fineberg, J., 2017. Brittle Fracture Theory Predicts
327 the Equation of Motion of Frictional Rupture Fronts, *Physical Review Letters*, **118**(12), 125501.
328 Uenishi, K. & Rice, J. R., 2003. Universal nucleation length for slip-weakening rupture instability under
329 nonuniform fault loading, *Journal of Geophysical Research: Solid Earth*, **108**(B1), 2042.
330 Walsh, J. J. & Watterson, J., 1987. Distributions of cumulative displacement and seismic slip on a single
331 normal fault surface, *Journal of Structural Geology*, **9**(8), 1039–1046.
332 Wei, S., Barbot, S., Graves, R., Lienkaemper, J. J., Wang, T., Hudnut, K., Fu, Y., & Helmberger, D.,

2015. The 2014 Mw 6.1 South Napa Earthquake: A Unilateral Rupture with Shallow Asperity and Rapid Afterslip, *Seismological Research Letters*, **86**(2A), 344–354.

Wu, B. S. & McLaskey, G. C., 2019. Contained Laboratory Earthquakes Ranging from Slow to Fast, *Journal of Geophysical Research: Solid Earth*, **108**(B1), 2019JB017865.